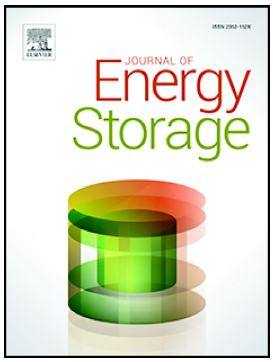

Synergistic effect of Echinops flower-like Copper sulfide@Cadmium sulfide heterostructure for high-performance all-solid-state asymmetric supercapacitor

Ranjith Balu, Anthoniammal Panneerselvam, R. Jothi Ramalingam, Gautham Devendrapandi, Surender Subburaj, S. Anand, Uma Shankar Veerasamy, Suganya Palani

PII: S2352-152X(23)01844-3

DOI: https://doi.org/10.1016/j.est.2023.108447

Reference: EST 108447

To appear in:

Received date: 5 March 2023

Revised date: 15 June 2023

Accepted date: 18 July 2023

Please cite this article as: R. Balu, A. Panneerselvam, R.J. Ramalingam, et al., Synergistic effect of Echinops flower-like Copper sulfide@Cadmium sulfide heterostructure for high-performance all-solid-state asymmetric supercapacitor, (2023), https://doi.org/10.1016/j.est.2023.108447

Synergistic effect of Echinops flower-like Copper sulfide@Cadmium sulfide heterostructure for high-performance all-solid-state asymmetric supercapacitor

Ranjith Balu [a, *], Anthoniammal Panneerselvam [b], R. Jothi Ramalingam [c], Gautham Devendrapandi [d], Surender Subburaj [e], S. Anand [f], Uma shankar Veerasamy [g] and Suganya Palani [h]

[a] Department of Physics, Saveetha School of Engineering, Saveetha Institute of Medical and Technical Sciences, Thandalam, Chennai, Tamilnadu 602105, India.

[b] Panimalar Engineering College, Chennai. Tamilnadu, India.

[c] Chemistry Department, College of Science, King Saud University P.O. Box. 2455, Riyadh 11451, Kingdom of Saudi Arabia.

[d] Department of Polymer Science, University of Madras, Guindy, Chennai, 602105, Tamilnadu, India.

[e] School of Engineering, Cardiff University, UK.

[f] Department of Polymer Science and Engineering, Korea National University of Transportation, Chungju 27469, South Korea.

[g] Department of Physics, Annamalai University, Chidambaram 608002, India.

[h] Department of Chemistry, C.K College of Engineering and Technology, Chellanguppam, Cuddalore-607003.

***Corresponding Authors**: Ranjith Balu (rbsnubio@gmail.com).

ABSTRACT

The fascinating properties of transition metal chalcogenides, including their distinctive morphologies, large surface areas, crystal structures, tunnel bandgaps, and structural stability, have led to a widespread acceptance of these compounds as ideal electrode materials for energy and environmental applications. Incorporating additional metal chalcogenides into metal chalcogenides to form a heterostructure can further enhance their electrical conductivity and provide them with more active sites. Herein, a simple hydrothermal method is used to synthesize a heterostructure CuS@CdS nanocomposite by integrating Copper sulphide and Cadmium sulphide. X-ray diffraction, Raman spectroscopy, and X-ray photoelectron spectroscopy were used to ascertain the phase formation and structural properties of the synthesized compounds. The electrochemical properties of the obtained materials were investigated. In a three-electrode configuration, a heterostructure CuS@CdS nanocomposite delivers high-specific capacitance

(543.6 Fg^{-1} at 1 Ag^{-1}) with excellent rate capability and outstanding cycling stability. A heterostructure CuS@CdS nanocomposite and activated carbon were employed as the negative electrode/positive electrode to construct an all-solid-state asymmetric supercapacitor device for real-world applications. This fabricated device exhibits a high energy density of up to 34.9 $Wh.kg^{-1}$ and power density of 798.1 $W.kg^{-1}$ and outstanding cyclic stability and retains up to 95.5 % over 3000 cycles. The outstanding results demonstrate that the CuS/CdS nanocomposite is an appropriate electrode material for a high-performance supercapacitor.

Graphical Abstract

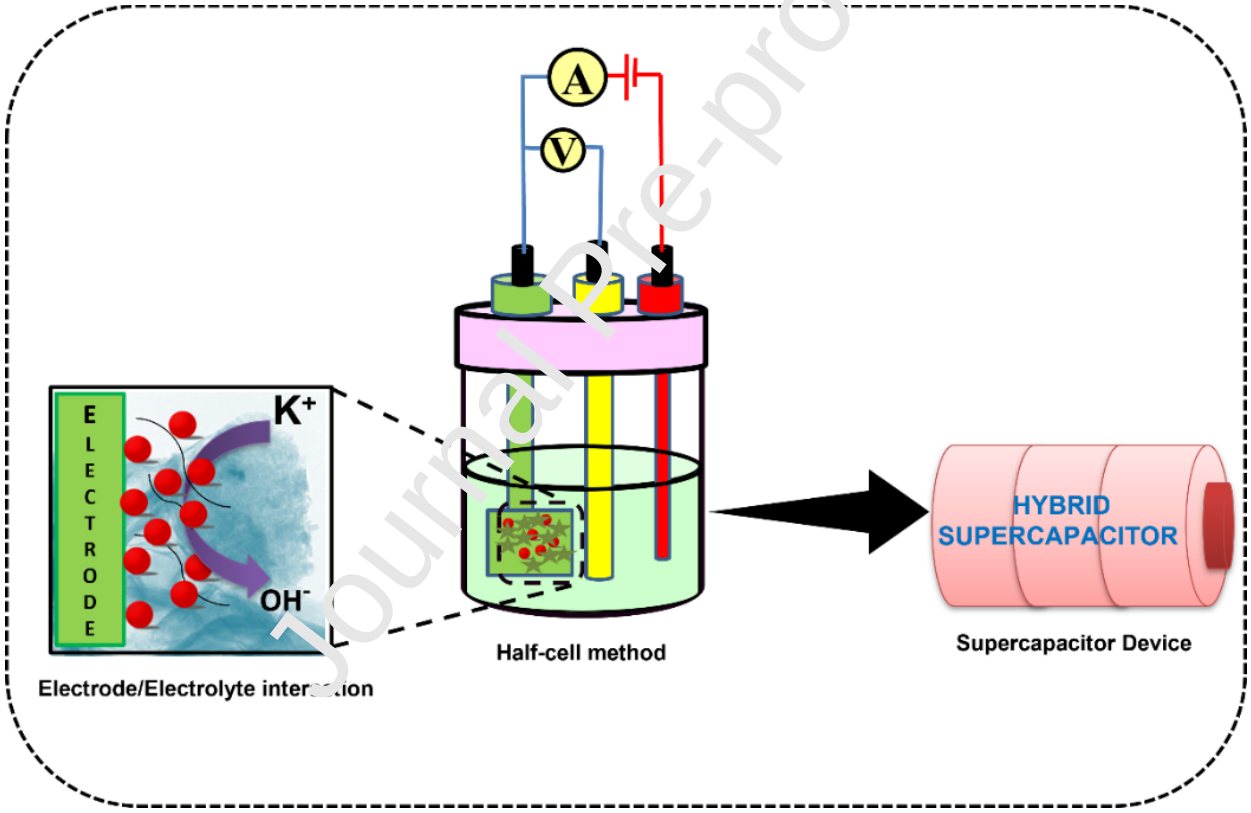

Keywords: Copper sulfide, Cadmium sulfide, heterostructures, electrochemical measurements, solid state supercapacitor device.

1 INTRODUCTION

With the tremendous development of electronic devices, environmental consequences associated with them have introduced new pathways for developing renewable energy sources

and storage technologies with promising prospects like high energy/power density, extended cycle stability, etc [1-5]. Among the various energy storage systems, batteries and supercapacitors (SCs) are the most well-known energy storage technologies with notable accomplishments for next-generation electronic devices [6]. Unfortunately, batteries have long been limited to ambient temperature because of their constraints of producing thermal fluctuations during the performance and having a low power density [7]. On the other hand, supercapacitors have fascinating characteristics such as being cost-effective, high-power density, prolonged cyclic stability, high columbic efficiency and eco-friendly as compared to other energy storage devices, namely, fuel cells and batteries [8-10]. Three types of supercapacitors-battery-type capacitors, pseudocapacitors, and electrochemical double-layer capacitors (EDLCs) can be distinguished from each other based on their storage mechanism. Moreover, three different types of supercapacitor devices can be commercialized: symmetric, asymmetric, and hybrid, these devices are sustainable energy storage with a variety of applications, including the automotive industry, hybrid electric cars, and military equipment [11]. Electrochemical double-layer capacitors' charge storage mechanism involves electrostatic energy storage; as a result, the electrode/electrolyte interfaces cause electrolyte ions to be absorbed and desorption at the surface of the electrode materials during the charge/discharge mechanism. In general, EDLC electrode materials are activated carbon (AC), graphene oxide, carbon nanotubes (CNT), and carbon black [12-14]. In the meantime, pseudocapacitors have electrochemically stored the energy; when the external voltage is applied on the electrode materials, the electrochemical reaction occurs between the electrode and electrolyte solutions because of the oxidation and reduction process between electrode materials and electrolyte solutions [15]. Pseudocapacitors utilize conducting polymers, and transition metal oxides/metal sulphides as their electrode components. [16,17]. In comparison to EDLCs, the pseudocapacitors electrochemical performances showed better specific capacitance and higher energy density. In battery-type supercapacitors, energy is stored electrochemically; during the redox reaction, anions/cations are intercalated into the crystal matrix of the active materials as a result of this phenomenon, the active materials are changed into a new phase [18]. Compared to EDLCs and pseudocapacitors materials, battery-type materials exhibit higher capacitance. Nevertheless, compared to batteries, supercapacitors have a lower energy density (10 Wh kg-1), which limits their use in several electronic devices. Hence,

the research community still has to be addressed to enhance the energy density of supercapacitors.

To increase the energy density of supercapacitors, it is necessary to address two key characteristics: the operating potential window (V) and the specific capacitance (Csp) of the device. Developing electrode materials with characteristic morphologies that have a wide surface area, a porous structure, and high electrical conductivity can increase the specific capacitance while employing the right electrolytes can improve the operating potential window (V) of the device. The energy density of supercapacitor devices is commonly increased using the techniques mentioned above. Recently, the research community has investigated and developed a variety of electrode materials to improve the overall performance of the supercapacitor device, but much more effort is still essential.

Noble metals have been employed as an electrode material for supercapacitors and, because of their various oxidation states, offer excellent capacitance than other materials. Due to their poisonous and restricted nature, many noble metals are not suitable for practical application. On the other hand, due to their additional valence states, morphologies, surface areas, and crystal structures, transition metal chalcogenides are widespread on Earth and exhibit outstanding physiochemical properties. These characteristics have the fascinating potential for use in a wide range of sectors, including energy conversion and storage [19]. For instance, ZnS, [20], CdS [21] and CoS [22] have drawn considerable interest because of their high-performance energy storage. Copper sulphide, one of several metal sulphides, has drawn a lot of attention from researchers because of its narrow band gap (1.63-1.87eV) energy, intriguing structure, morphologies, an abundance of electronic and defect states, and environmental friendliness. As a result, it is employed in a vast array of applications, including energy conversion and storage, switches, optical filters, chemical sensors, catalysis, and many more. Besides, due to the valance state of 3p in the sulphur S atom's role as an electron acceptor, CuS has been exploited as a suitable electroactive material in recent years [23]. Hence, CuS nanoparticles effectively interact with other materials to form heterostructures, which will change the characteristics of the material such as surface area and band gap variation and so improve its electroactive capabilities. Because of their excellent electrical conductivity, rich valence state, and smaller bandgap, CuS-based heterostructures nanocomposite materials, such as CuS/CoS [24] and CuS/MnS [25], are

suitable for energy storage applications (0 to 2 eV). The superb n-type semiconductor cadmium sulphide (CdS) has numerous exceptional physicochemical characteristics. It has prospective uses in several scientific domains, including solar cells, photocatalysis, and light-emitting diodes for large-screen displays [26]. Many studies have documented the existence of CdS nanostructures with various morphologies, including nanorods, due to an overabundance of cadmium atoms, it has sulphur vacancies, which is what gives it its semiconducting properties [27]. To address the issues, it is essential to have a rational structure design in order to increase the storage performance. CuS-based heterostructures play a significant role in improving the performance of storage systems among all techniques. As one of the reasons for this, there are a number of active components utilized in the storage of metal ions, all working synergistically in order to combine the advantageous characteristics of each structure without the disadvantages, it is easy to build p-n junctions at the boundary between CuS and CdS, which can assist the movement of photoexcited electrons from CuS to CdS due to the generation of internal electric fields.

Considering the above-mentioned discussions, it was decided to synthesize CuS nanoparticles decorated CdS (CuS/CdS) heterostructure using a simple hydrothermal approach. The morphologies, crystal structures, porous nature, and thermal characteristics were examined to evaluate the physicochemical parameters. In addition, a half-cell configuration was employed to investigate the electrochemical performances of the obtained materials. The resultant CuS/CdS nanocomposite electrode exhibits prolonged cyclic stability and higher specific capacitance than CuS and CdS nanoparticle electrodes. Furthermore, a complete solid-state asymmetric supercapacitor (AC||CuS/CdS) device was designed. The fabricated ASC provided improved cyclic stability along with higher energy and power densities. The interaction between the nanomaterials CuS and CdS ultimately provides the ASC with its enhanced performance. As a result, the constructed all-solid-state supercapacitor device exhibits an outstanding electrochemical performance with a unique combination.

2 EXPERIMENTAL SECTIONS

2.1 Materials

The following substances were acquired from Sigma-Aldrich: sodium sulphide nonahydrate ($Na_2S_9H_2O$), cadmium (II) acetate monohydrate ($C_4H_8CuO_5$), and copper (II)

acetate dihydrate ($Cd(CH_3COO)_2$ $2H_2O$). Merck Chemicals provided the polyvinylidene difluoride (PVDF), carbon block, and N-methyl pyrrolidone (NMP). The Millipore water purification facility provided deionized water that was used for synthesis and cleaning.

2. Preparation of CuS@CdS core-shell nanocomposite

In this study, a straightforward one-pot hydrothermal technique was used to synthesize a CuS@CdS core-shell nanocomposite. The precursors Copper (II) acetate monohydrate ($C_4H_8CuO_5$), Cadmium (II) acetate dihydrate ($Cd(CH_3COO)_22H_2O$), and thiourea (CH_4N_2S) were combined in a 1:1:2 ratio for Cu, Cd, and S, and then dissolved in 60 ml of water while being continuously stirred for 60 minutes. The resulting solutions were then put into an autoclave that was lined with Teflon. For 24 hours, a sealed autoclave was held at 180 °C in a furnace. The black precipitate was produced and repeatedly rinsed with 100% ethanol and deionized water after cooling to room temperature. To remove the moisture of the materials, it was dried in a vacuum oven at 80 °C overnight to obtain the CuS@CdS nanocomposite. In the synthesis of CuS and CdS nanoparticles, a similar method was followed without adding the cadmium and copper precursor. The formation of the CuS@CdS nanocomposite is described in the figure. 1

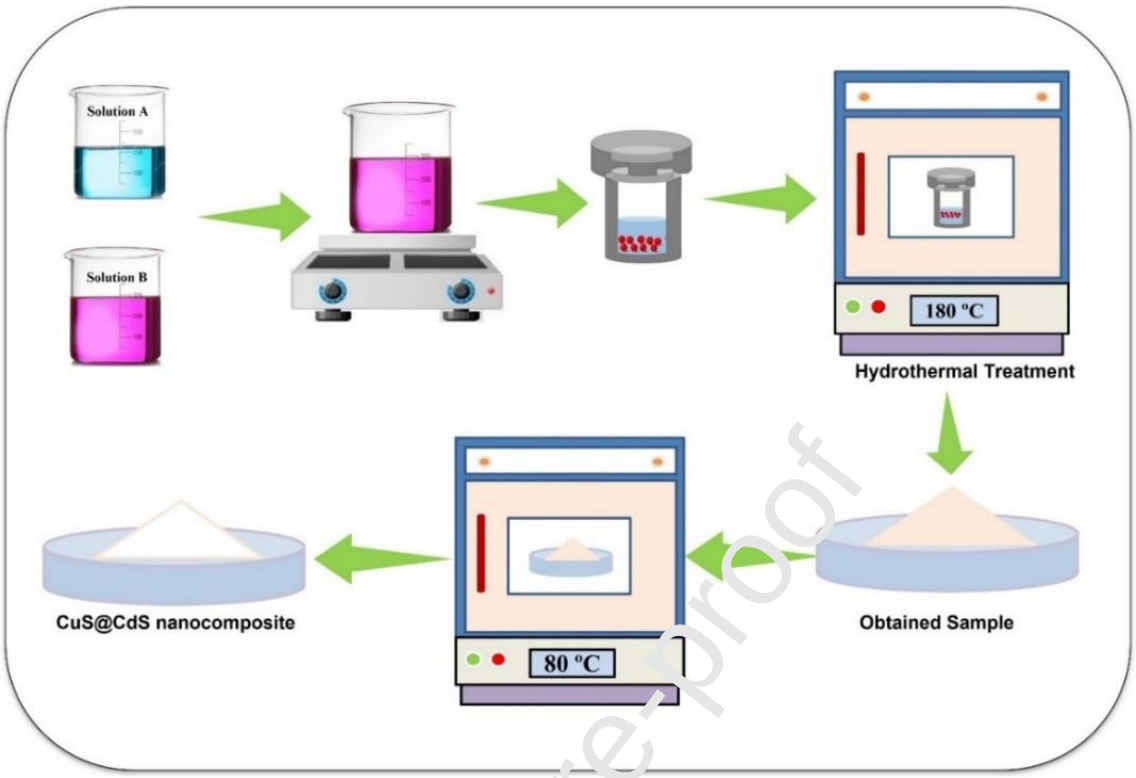

Scheme.1. Schematic illustration of the preparation of CuS@CdS nanocomposite

2.5 Materials Characterization

Powder X-ray diffraction was used to study the phase identification (PANalytical, using Cu K radiation, =0.15405 nm). Thermo Scientific K-Alpha X-ray photoelectron spectroscopy (XPS) and Fourier transforms infrared spectroscopy were used to assess the chemical composition and functional groups of the materials. SEM (Zeiss 18 SEM) and transmission electron microscopy were used to examine the morphologies and chemical content of the prepared materials. N_2 adsorption-desorption isotherms were utilized to estimate parameters, and then the Brunauer-Emmett-Teller method was used to calculate the specific surface area and pore size distribution using the QUADRSORP SI analyzer.

2.6 Electrochemical measurements

The as-synthesized CuS@CdS core-shell nanocomposite, activated carbon, and polyvinylidene fluoride were mixed in a weight ratio of 80:10:10 to construct the working electrode. The resultant slurry was then applied to a processed Ni foam substrate of 1cm ×1cm and it was dry for 12 hours at 80 °C in the oven, then it was observed that there was around 2 mg

of active electrode materials on the nickel foam. The electrochemical methods of cyclic voltammetry (CV), galvanostatic charge/discharges (GCD), and cyclic stability were carried out in the potential window of 0 V to 0.65 V. The following equation was used to determine the specific capacitance and areal capacitance from cyclic voltammograms and galvanostatic charge discharges.

Specific capacitance from CV

$$C_{sp} = \int \frac{\mathrm{Idv}}{\mathrm{m\upsilon\ V}} \quad (1)$$

Specific capacitance from GCD

$$C_{sp} = \frac{I \times \Delta t}{m \times \Delta V} \quad (2)$$

Where, *I* represents the applied current (A), m signifies the mass of the active material (g), V denotes the potential window (V), and t denotes the discharge period of one cycle (s). Csp denotes the specific capacitance of the electrode (F/g).

2.7 Fabrication of the all-solid-state asymmetric supercapacitor device (ASC)

To developing electrode materials for commercial applications, an all-solid-state asymmetric supercapacitor was fabricated. In a full-cell setup, activated carbon and the nanocomposite were used as the anode and cathode, respectively. The aforementioned method was used to prepare each electrode. The whatman paper and fabricated electrodes were immersed in a prepared 3M KOH aqueous gel electrolyte solution. The all-solid-state supercapacitor was constructed with an anode and a cathode. The whatman paper was firmly sealed and acted as a separator between the electrodes. The electrochemical properties of the all-solid-state asymmetric supercapacitor device were evaluated. The device specific capacitance as well as its energy and power density were calculated using the formulas below.

$$C_{sp} = \frac{I \times \Delta t}{\Delta V \times m} \quad (3)$$

$$E = \frac{Csp \times \Delta V^2}{2} \quad (4)$$

$$P = \frac{\Delta V \times I}{2m} \quad (5)$$

In this equation, E is the energy density (Wh kg^{-1}), P is the power density (W kg^{-1}), I is the discharge current (A), t is the discharge duration (s), and V is the cell operating potential (V) (g).

3 RESULTS AND DISCUSSION

3.1 Structural analysis

The phase identification and crystal structure of as-prepared materials including CuS, CdS, and CuS@CdS core-shell nanocomposite was evaluated using an X-ray diffractometer. The obtained X-ray diffraction patterns of the materials are depicted in Fig.1 (a). According to JCPDS data (JCPDS No. 06-0464), the obtained CuS nanoparticles diffraction peaks 2 at 27.80, 29.32, 31.81, 32.87, 48.15, 52.90, and 59.32 are interpreted as reflecting the hexagonal crystal structure of CuS. [22]. The conventional hexagonal phase crystalline structure with (a = 4.121, b = 6.682) the lattice parameter of CdS NPs can be ascribed to the diffraction peaks at 23.907, 25.807, 27.982, 43.681, 47.839, and 51.824, corresponding to the (100), (002), (101), (110), (103), and (112) planes (JCPDS No. 41-1049) [21]. Interestingly, the P-XRD pattern of the CuS@CdS nanocomposite was correlated including both CuS and CdS diffraction peaks, which is validating the formation of CuS@CdS nanocomposite. According to the results, the CuS@CdS nanocomposite was formed with a well-refined crystalline structure without any impurity peaks. The average crystallite size of the electrode materials was determined using the Debye-Scherrer formula.

$$D = \frac{0.9\,\lambda}{\beta cos\theta} \quad (6)$$

Where K is the slope factor (0.9), is the Bragg diffraction angle, D is the average crystalline size of the materials, λ is the X-ray beam wavelength, and is β is the full width at half maximum (FWHM). It was determined that the average crystallite size of CuS, CdS, and CuS@CdS nanocomposite was 42.9 nm, respectively.

Raman spectroscopy was used to determine the crystallization nature and structural defects of the materials. Fig. 2 (b) illustrates the results of an investigation into the 200-2000 cm^{-1} region of the prepared materials Raman spectra at ambient temperature. Two distinguishable

peaks were seen in the CuS nanoparticles. The Cu-S bond's vibration mode causes the first peak to be positioned at 270 cm^{-1}, while the covalent S-S bonds between S_2 ions vibrational mode are responsible for the second peak at 474 cm^{-1} [28]. CdS nanoparticles have three prominent peaks: a prominent intense peak at 302 cm^{-1}, which corresponds to the fundamental optical phonon mode (LO), and two broad peaks at 603 and 903 cm^{-1}, which are associated with the first and second overtone modes (2LO and 3LO) of CdS nanoparticles [29]. Raman spectra of CuS and CdS peaks were observed in the CuS@CdS nanocomposite, which indicates the formation and confirmes the existence of CuS and CdS nanoparticles, which is corroborated by XRD data [30].

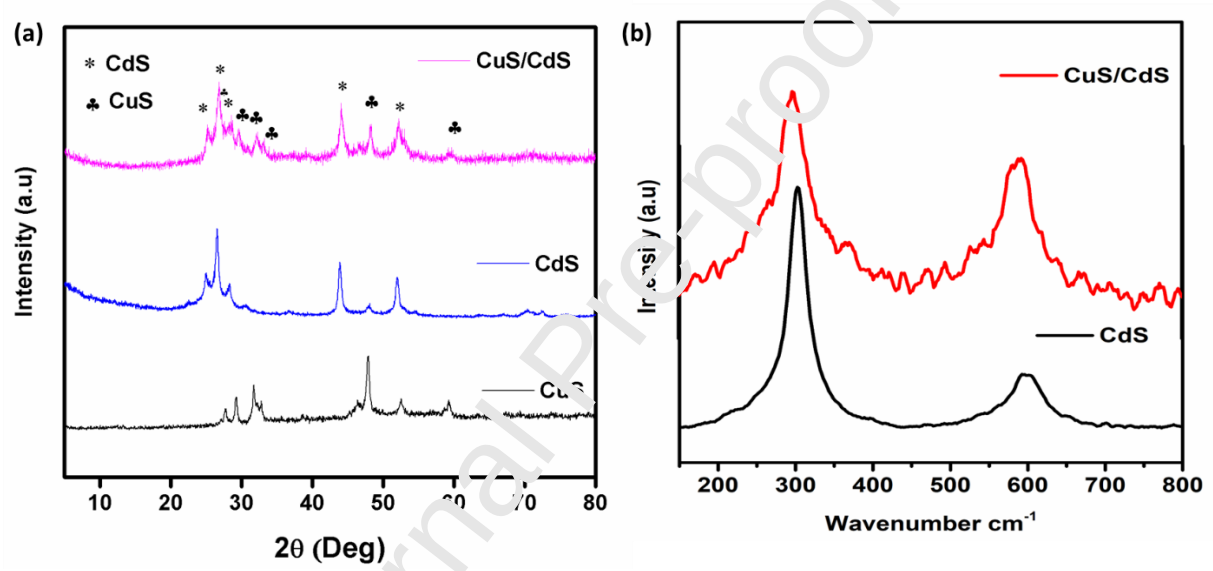

Fig.1 (a) XRD patterns of CuS, CdS, and CuS@CdS nanocomposite (b) Raman spectrum of CdS, and CuS@CdS nanocomposite.

The chemical composition and chemical oxidation states of the CuS@CdS nanocomposite were identified using X-ray photoelectron spectroscopy (XPS) analysis. The formation of the CuS@CdS nanocomposite is confirmed by the full survey spectrum of the material, which reveals the existence of Cd, Cu, and S elements and is also well-matched with our experiment. According to Fig. 2 (b), the core level spectra of Cu 2p depict two distinct peaks at 932.11 eV and 951.65 eV, which correspond to the Cu $2p_{3/2}$ and Cu $2p_{1/2}$ states, respectively. These peaks represent the oxidation state of Cu^{2+}. A confirmation of the chemical oxidation state of Cd^{2+} in the CuS@CdS nanocomposite shown in Fig. 2(c) is provided by the high-resolution core level spectrum of Cd 3d, which displays two prominent peaks at 405.56 eV and 412.12 eV,

respectively, corresponding to Cd 3d $_{5/2}$ and Cd 3d $_{3/2}$ energy states. Moreover, Fig. 2 (d) depicts the core level spectrum of S 2p and demonstrates two peaks that are related to S^{2-} and are positioned at energy levels of 162.14 and 163.31 eV, corresponding to S $2p_{3/2}$ and S $2p_{1/2}$ respectively, according to the XPS analysis, the surface composition of CuS@CdS nanocomposite is composed of Cu^{2+}, Cd^{2+} and S^{2-} energy states respectively, which is confirming the formation of CuS@CdS nanocomposite and corroborated with the XRD results [31].

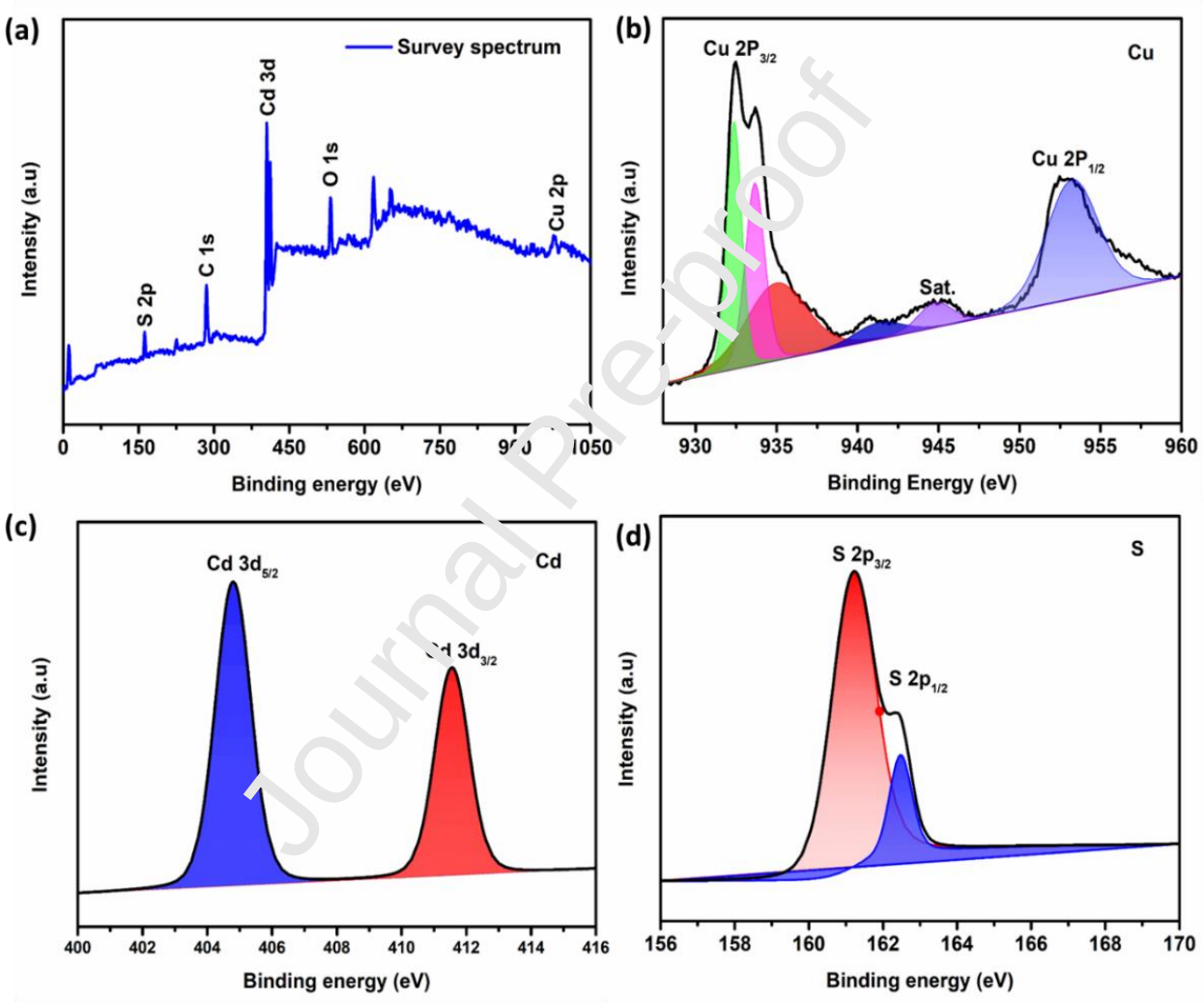

Fig.2 XPS survey spectrum of (a) CuS/CdS nanocomposite (b-d) High-resolution XPS scans of Cu 2p, Cd 3d and S 2p, respectively.

3.2 Morphological and elemental analysis

Scanning electron microscope (SEM) analysis was employed to examine the surface morphologies and microstructures of prepared materials. Fig.3. illustrates the morphological details of the as-prepared components. As depicted in Fig. 3 (a&b), the obtained CuS nanoparticles demonstrate a ball-like structure, that was assembled by the interdigitation of groups of ultrathin nanosheets. The CdS nanoparticles had uneven morphologies and were made up of aggregates of granules distributed in a variety of orientations which is revealed in Fig. 3 (d&e). The unique morphologies of CuS@CdS nanocomposite have been optimized by choosing the appropriate sulfur precursor. Interestingly, the CuS and CdS nanoparticles have been distributed in a variety of orientations to form a stable some ball-like nanocluster structure, which is shown in Fig. 3 (g&h). The irregular shape CdS nanoparticles and CuS ball-like structure morphologies were present here which is indicating the formation of CuS/CdS nanocomposite. The obtained morphologies enhance the nanocomposite materials surface area due to the synergistic effect of CuS and CdS nanoparticles, which will increase their active sites and favorable for remarkable redox reactions. The obtained nanocomposite materials possess high electrochemical active sites and will increase the electrode/electrolyte interaction, hence resulting in low resistance and outstanding electrochemical performances. EDAX analysis was used to determine the chemical composition and elemental identification of the components. The Cu and S peaks in Fig. 3 (e) correspond to CuS, demonstrating the formation of CuS nanoparticles. The observed peaks Cd and S in Fig. 3 (f) indicate the formation of CdS nanoparticles. In the context of the CuS@CdS nanocomposite, both correlating peaks for Cu, Cd, and S were observed which is indicating nanocomposite formation as shown in Fig 3 (i). The insert table provides the constituent element's weight percentage and atomic percentage.

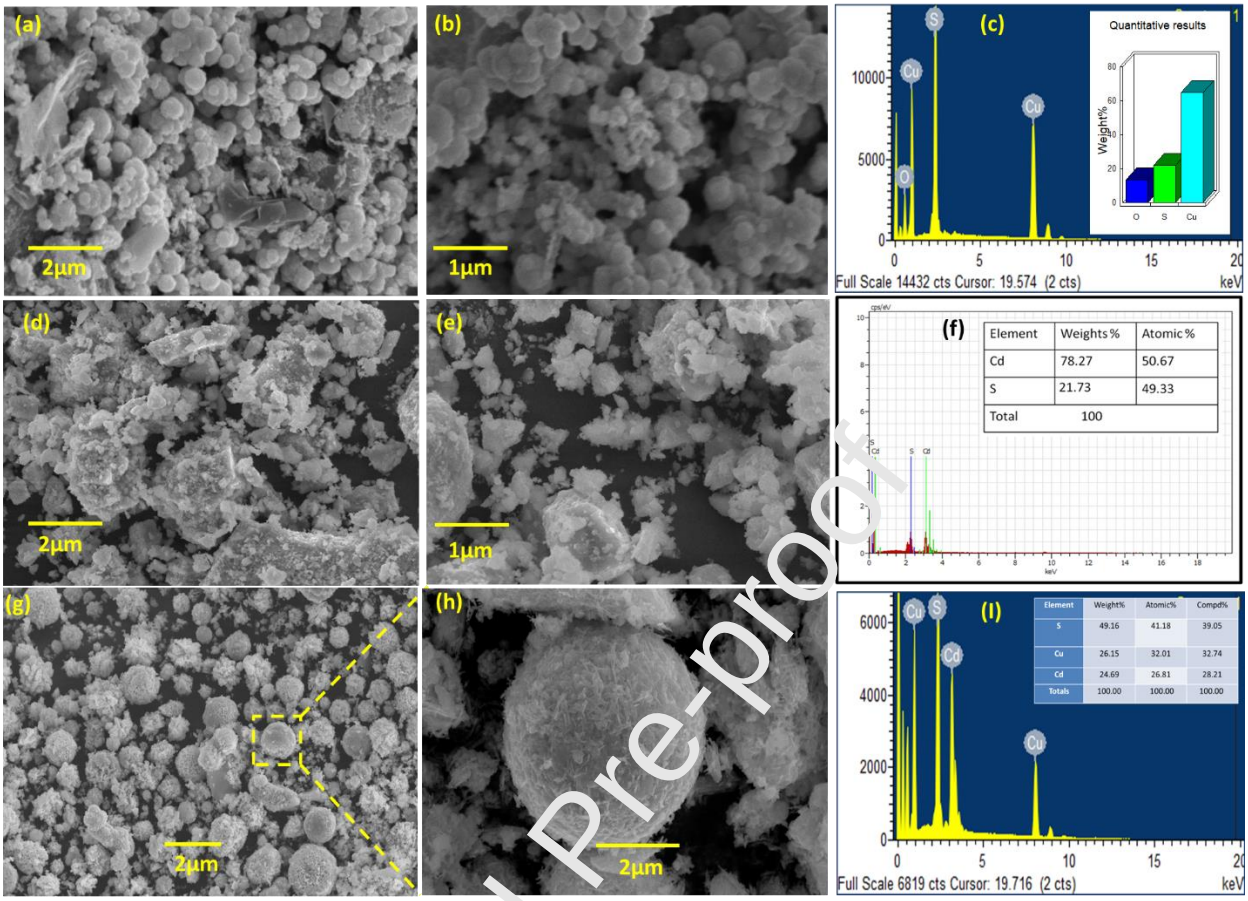

Fig.3 SEM images of (a-c) CuS and (d-f) CdS nanoparticles and (g-i) CuS@CdS nanocomposites and its corresponding EDAX spectrum.

Furthermore, a Transmission electron microscope (HRTEM) was used to examine the detailed morphology and inner nanostructure of CuS@CdS nanocomposites. Fig. 4 (a-c). depicts the various magnifications of CuS@CdS nanocomposites obtained images. From these results, Intriguingly, ball-like structures ornamented with irregular-shaped of CdS nanoparticles were found here, and also CuS small ball-like structure have been have been dispersed in a range of orientations which is confirming the construction of CuS/CdS nanocomposite form a stable cluster structure, which shows strong agreement with the SEM data. To gain a better understanding of the crystalline structure of the composite materials has been subjected to selected-area electron diffraction (SAED), as shown in Fig. 4 (d). The obtained results demonstrate a series of diffused Debye-Scherer rings, which correspond to the CdS and CdS, which is in accordance with results from the XRD. These results confirmed the synergetic effect of CuS/CdS nanoparticles. The obtained morphologies enhance the electrode/electrolyte

interaction by increasing the number of active sites and structural stability. Also, the structure's enhanced surface area could facilitate redox reactions during electrochemical processes.

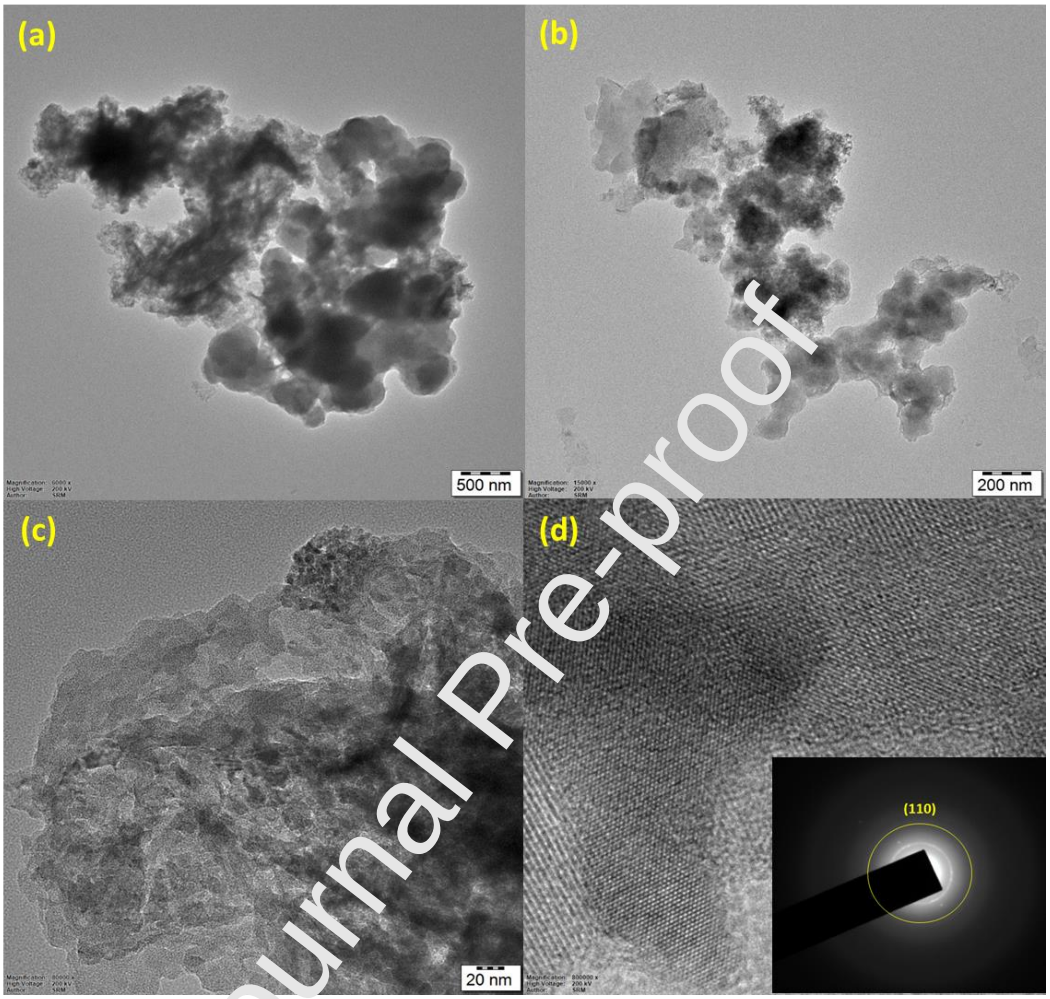

Fig.4 HRTEM image of (a-c) CuS@CdS nanocomposite with various nm (d) CuS@CdS nanocomposite showing lattice images with measured d value.

3.3 Surface area analysis

The surface area and porous nature of the compounds play a prominent role in the electrochemical performances. The Brunauer-Emmett-Teller (BET) technique was used to determine the specific surface area and pore size distribution of the materials. The nitrogen adsorption-desorption isotherms and pore size distributions of the initially synthesized materials CuS, CdS, and CuS@CdS nanocomposite are shown in Fig. 5, respectively. According to Fig. 5(a), all of the obtained materials' nitrogen adsorption-desorption isotherms demonstrated typical

IV isotherms with significant H_3-type hysteresis loops, which are associated with a mesoporous structure (2–50 nm) [32]. The prepared materials CuS, CdS, and CuS@CdS nanocomposite have attained surface areas of 52.5 m^2g^{-1}, 20.8 m^2g^{-1}, and 40.3 m^2g^{-1}, respectively. Moreover, the obtained materials BJH pore size distribution is demonstrated in Fig. 5 (b). The average pore-size distribution of respective mesoporous materials CuS/CdS nanocomposite, CuS and CdS nanoparticles corresponds to 3.67 nm, 7.52 nm and 9.17 nm respectively. From these results, the CuS@CdS nanocomposite materials demonstrated mesoporous structures as well as larger pore volume and high surface area compared to CuS and CdS nanoparticles that were originally acquired. CuS@CdS nanocomposite's enhanced specific surface area and extremely porous structure enable more active sites to participate in redox reactions during electrochemical performances. Especially, the synergistic effect of CuS and CdS composite greatly improves the active sides in the CuS@CdS core-shell heterostructure by enabling more channels for ion/electron transport kinetics, which enhances the material's specific capacitance values and the performance of supercapacitors.

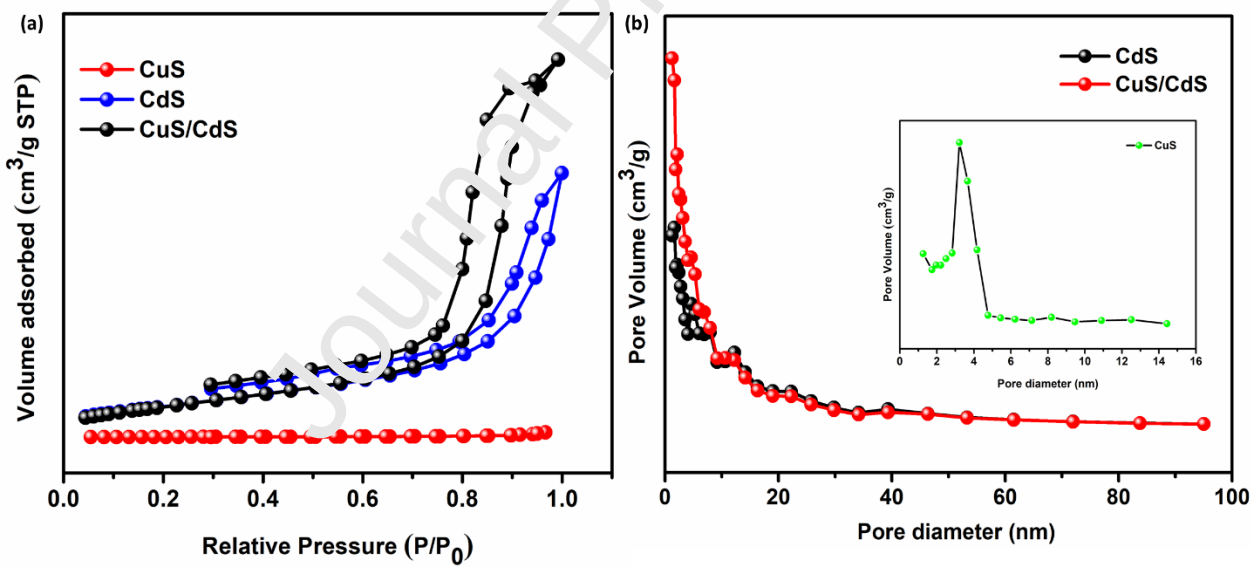

Fig.5. (a) N_2 adsorption-desorption isotherm and (b) pore size distribution of CuS, CdS, and CuS@CdS nanocomposite.

3.4 Functional groups and Thermogravimetric analysis

As-prepared materials functional groups were examined using Fourier Transform-Infrared (FT-IR) spectroscopy, as illustrated in Fig. 6 (a). For CuS nanoparticles, the weak vibration peak appeared at 630 cm^{-1}, which corresponds to the vibrational stretching of the Cu-S bond [33]. The stretching vibration of hydroxyl (O-H) is attributed to the occurrence of a broad vibration peak at around 3422 cm^{-1}. The Cd-S stretching vibration is attributed to the intense vibration peaks at 1395, 1106, and 862 cm^{-1}. The stretching vibration of the CdS bond is responsible for the existence of prominent vibration peaks at 1384 and 1128 cm^{-1}. At a wavelength of 2921 cm^{-1}, the C-H bond stretching vibration was noticed. The stretching vibration of the O-H bond causes the wide vibration peak at approximately 3425 cm^{-1}, which denotes the formation of CdS nanoparticles [34]. CuS and CdS nanoparticles are formed in the CuS@CdS nanocomposite, which is indicated by the identification of both CuS and CdS corresponding peaks. These results from XRD and Raman are also consistent with this approach [35].

The thermal stability of the materials was evaluated using thermogravimetric analysis (TGA), which involved heating the materials from room temperature to 800 °C at a rate of 10 °C/min. Fig. 6 (b) clearly shows the apparent weight reduction for CuS, CdS, and CuS@CdS nanocomposite. All three materials demonstrated various thermal behaviors according to their functional groups. Because of the elimination of the water molecule and moisturizing, the minimal weight loss for CuS nanoparticles has occurred below 100 ºC. CuS nanoparticle phase transformation caused a moderate weight loss from 200 ºC to 300 ºC, whereas exothermic reactions that resulted in CuS oxidizing into CuO and $CuSO_4$ provided a significant weight gain at 300 ºC. The gradual weight loss between 500 ºC to 800 ºC was then observed and corresponded to the decomposition of $CuO.CuSO_4$ produces CuO [22]. Due to the removal of moisture and water molecules, the CdS nanoparticles exhibit a minimum weight loss of up to 100 ºC. Thereafter, a 10% weight reduction was gradually achieved to 800 ºC [21]. Furthermore, the as-prepared CuS@CdS nanocomposite demonstrated minimum weight loss observed at less than100 ºC due to the dissociation of water molecules and moisture and then the weight loss is approximately 350 ºC, which might be phase transformation of CuS nanoparticles in the CuS@CdS nanocomposite. In addition, suddenly weight increased up to 130 w% at 350 ºC due

to CuS converted into CuO and $CuSO_4$ and it withstood up to 700 ºC. Furthermore, the sudden weight loss observed at 700 ºC to 800 ºC due to $CuSO_4$ converted into CuO. In comparison to pure CuS nanoparticles, the CuS@CdS nanocomposite showed exceptional thermal stability. The CuS@CdS nanocomposite has increased thermal stability due to the presence of CdS nanoparticles. The CuS@CdS nanocomposite has excellent thermal stability due to the presence of CdS nanoparticles. CuS@CdS nanocomposite's high thermal stability will assist in maintaining cyclic stability for a prolonged period during the electrochemical performance.

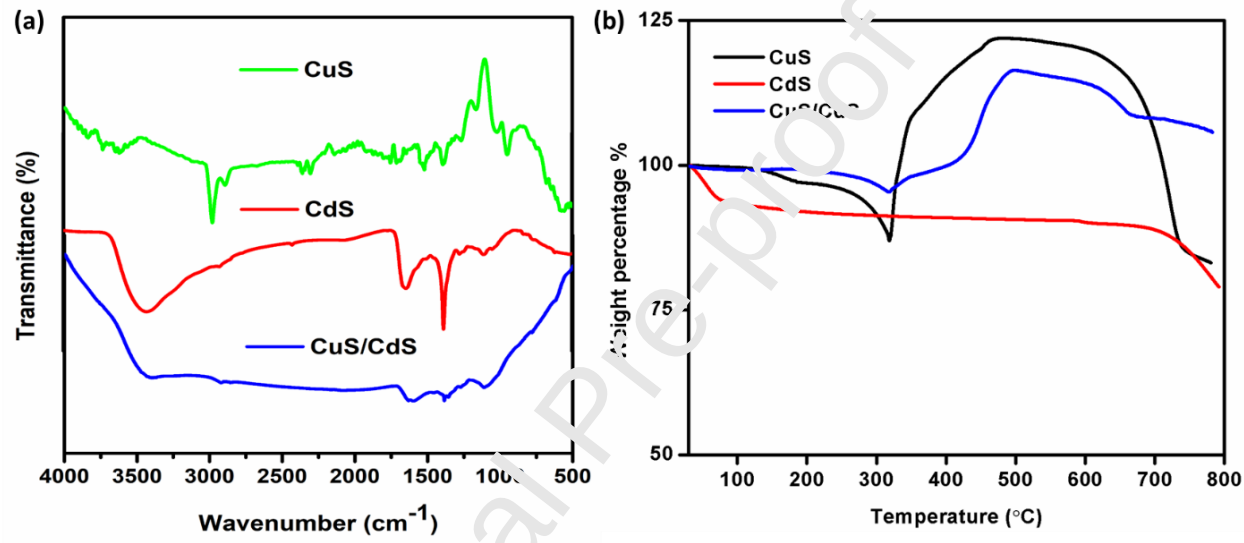

Fig.6. (a) FTIR spectrum of CuS, CdS, CuS@CdS nanocomposite, and (b) TGA spectrum of CuS, CdS, CuS@CdS nanocomposite.

3.5 Optical properties analysis

The optical characteristics of the materials as-prepared were investigated using DRS UV-Vis spectrophotometry, and the results of the measured absorption spectra are shown in Fig. 7 (a). The CdS nanoparticles absorbance spectrum was observed at around 480 nm as a result of charge transfer between the valence band to the conduction band ($S2^-$ to $Cd2^+$). In addition, to CuS nanoparticles, a significant absorption spectrum was observed at 664 nm due to the d-d transition of $Cu2^+$. In the instance of CuS@CdS nanocomposite, it exhibits that a wide absorption band was identified at 554 nm, indicating the decorating of the CuS over the CdS nanoparticles and also confirming that the CuS is not integrated into the crystal structure of CdS

nanoparticles. [36]. The corresponding energy band of the materials have been evaluated using the Tauc plot.

$$(\alpha h\nu)n = A(h\nu - Eg) \quad (7)$$

The bandgap (Eg) values of the CdS and CuS nanoparticles were found to be 2.3 eV and 1.7 eV, respectively as shown in Fig. 7 (b). Using the abovementioned relation, the band gap energy of CuS@CdS nanocomposite was calculated, and the result was 1.75 eV which is lower than that of CdS and greater than CuS [37]. This result suggests that the intermediate band gap could play a key role in the initialization of the separation of electrons and holes, which significantly improves redox reaction during the electrochemical performance

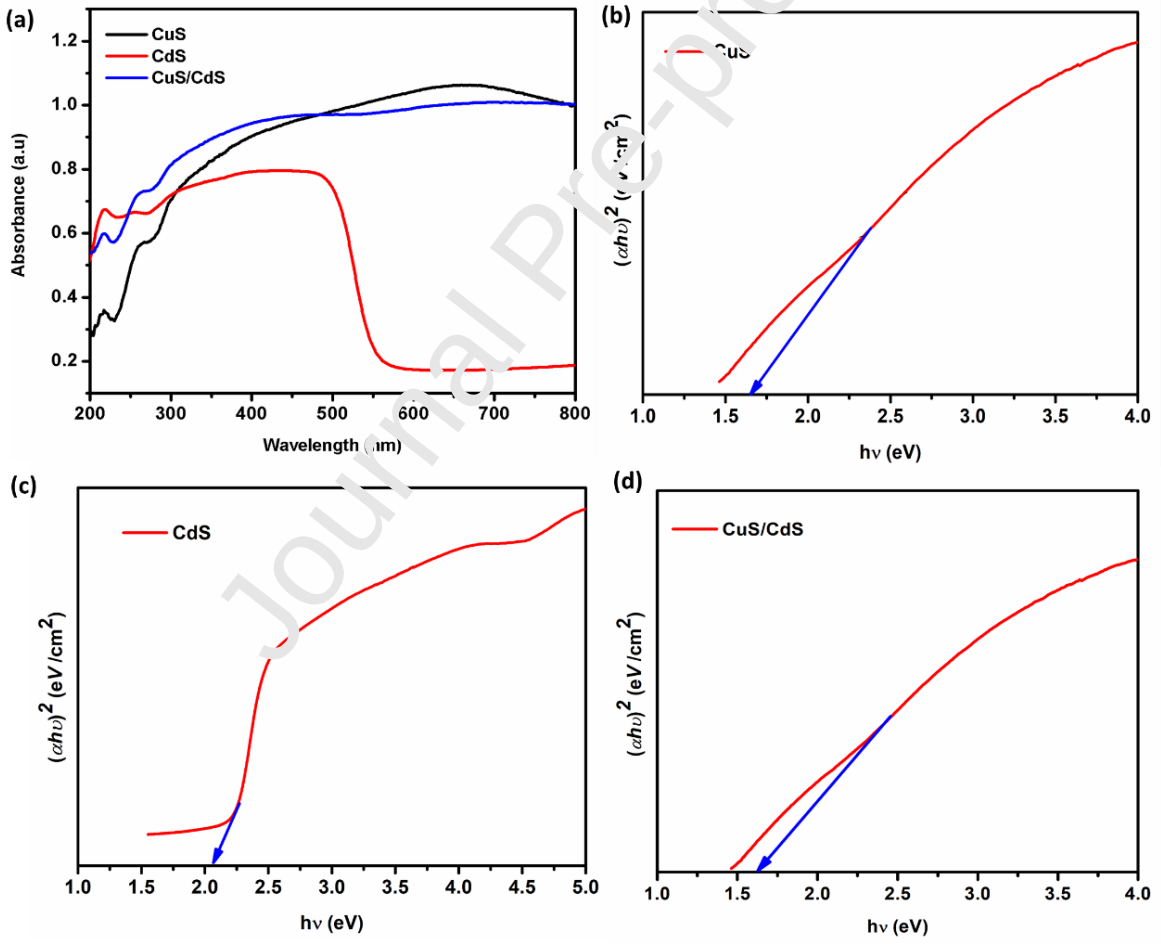

Fig.7. (a) DRS UV-vis spectrum of CuS, CdS, CuS@CdS nanocomposite and its corresponding Optical band gap of (b) CuS, (c) CdS, and (d) CuS@CdS nanocomposite.

3.8. Electrochemical measurements

To examine the electrochemical performances of the fabricated electrodes, Electrochemical impedance spectroscopy (EIS), galvanostatic charge-discharge (GCD), and cyclic voltammetry (CV) was employed in a half-cell technique using an aqueous (3M KOH) electrolyte solution. The fabricated electrodes CuS, CdS, and CuS@CdS nanocomposite comparative cyclic voltammetry curves at a scan rate of 100 mVs^{-1} are shown in Fig. 8. In these curves, CuS@CdS nanocomposite exhibits a larger integral area than the other two prepared materials. At a potential window of 0-0.65 V, the CV curves of the constructed electrodes, such as CuS, CdS, and CuS@CdS nanocomposites, were investigated at various scan rates, as shown in Fig. 8 (b-d). In the alkaline electrolyte medium, all three electrodes exhibited oxidation and reduction peaks indicating their pseudocapacitive nature [33]. When the scan rates are increasing while the shape of the CV curves also increased and the corresponding oxidation and reduction peaks were shifted evenly to the right and left sides due to the electrochemical polarization, these behaviors indicate that the materials are capable of operating at high rates. The entire sweep rates of all materials possess the redox peaks due to the reversible redox reaction. Moreover, the synergistic effect of both materials could also be attributed to the excellent performance of the CuS@CdS nanocomposites.

Faradic Reaction:

$$CuS + OH^- \leftrightarrow CuSOH + e^- \quad (08)$$

$$CuSOH + OH^- \leftrightarrow CuSO + H_2O + e^- \quad (09)$$

$$CdS + OH^- \leftrightarrow CoSOH + e^- \quad (10)$$

$$CdSOH + OH^- \leftrightarrow CoSO + H_2O + e^- \quad (11)$$

Non-Faradaic Reaction:

$$(CuS@CdS)\ surface + K^+ + e^- \leftrightarrow (CuS@CdS)\ surface \quad (12)$$

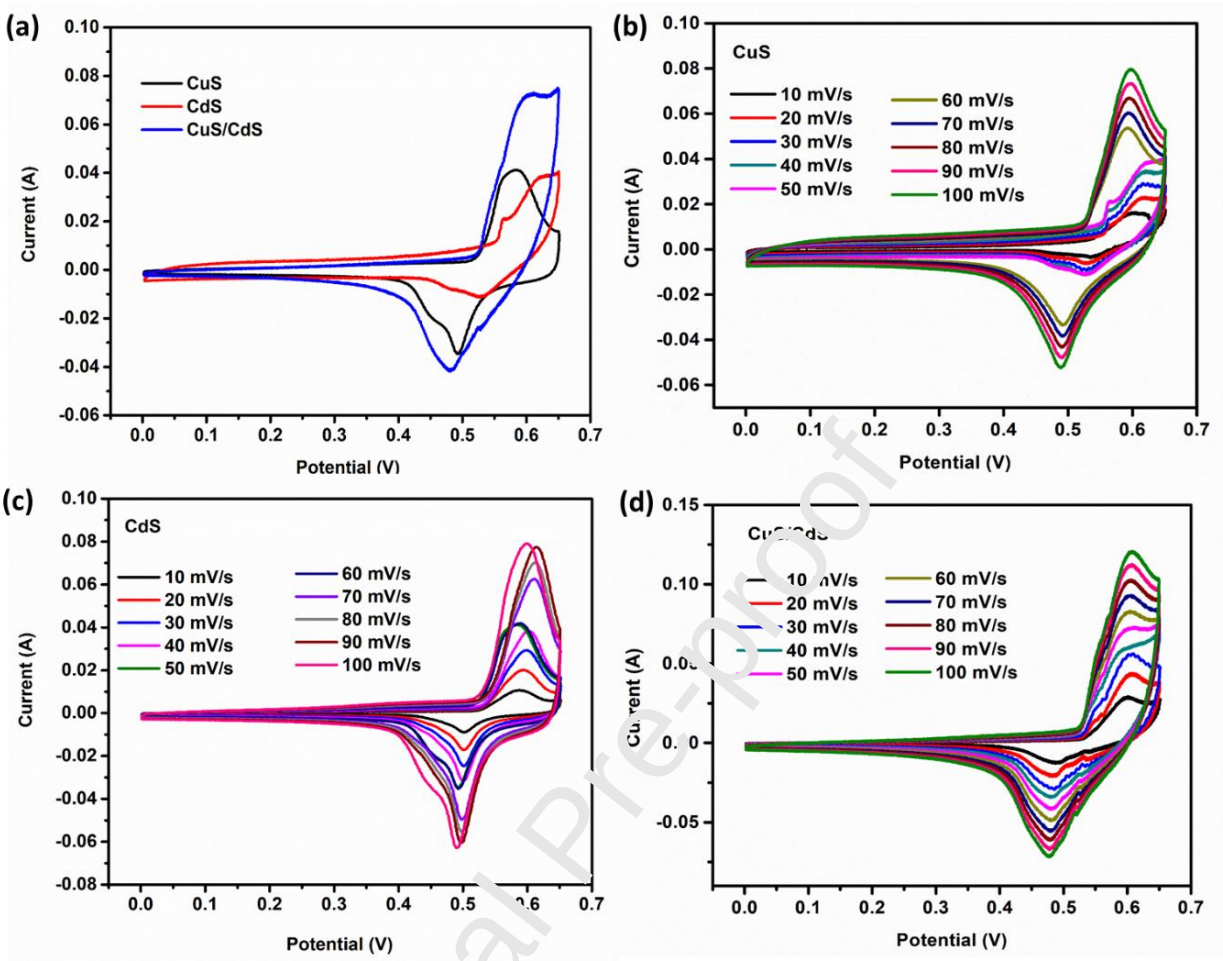

Fig.8. Cyclic voltammetry response of (a) CuS, CuS, and CuS@CdS nanocomposite at a scan rate of (b) pure CuS nanospheres, (c) CdS nanoparticles, and (d) CuS@CdS nanocomposite over various scan rates.

Galvanostatic charge-discharge (GCD) measurements are one of the widely used methods for assessing the capacitance properties of electrode materials. The GCD curves of the obtained electrodes such as CuS, CdS and CuS@CdS nanocomposite were measured at different current densities (1-15 Ag^{-1}) with a potential window of 0-0.65 V. Fig. 9 (a) demonstrates the comparison GCD curves of all three electrodes at a current density of 1 Ag^{-1}. As expected, the CuS@CdS nanocomposite electrode exhibits a longer discharging time compared to the other two materials. The GCD curves of all three electrodes demonstrate a non-linear shape during the charge/discharge processes which suggest that the redox mechanism occurs between both the electrolyte and the electrode. All three materials results are corroborated with the CV test. The

GCD curves of CuS, CdS and CuS@CdS nanocomposite were obtained at various current densities which are demonstrated in (Fig. 9b), (Fig. 9c) and (Fig. 9d) respectively.

According to equation (2), the specific capacitance (Cs) of the electrode materials was calculated from the discharge curve, and the results are summarized in Table. S1. Following these results, the specific capacitance values for all three materials decreased as the current density increased, which is consistent with the inverse relationship between the two. The minimum capacitance of the materials is caused by OH^- ion's inability to permeate into the internal surface of the electrode at high current densities during the charge/discharge operation. Fig.10 (a). compares the specific capacitances of nanocomposite materials constructed of CuS, CdS, and CuS@CdS. (c). The CuS@CdS nanocomposite outperformed the other two electrode materials, achieving a maximum capacitance of 543.6 Ag^{-1} at a current density of 1 Ag^{-1}. CuS@CdS nanocomposite's high specific capacitance is induced by their large surface area and conducting nature. A major component of the overall performance can be attributed to the synergetic effect of CuS and CdS nanoparticles to form a stable structure that enhances the high surface area and reduces diffusion and migration paths for electrolytes ions.

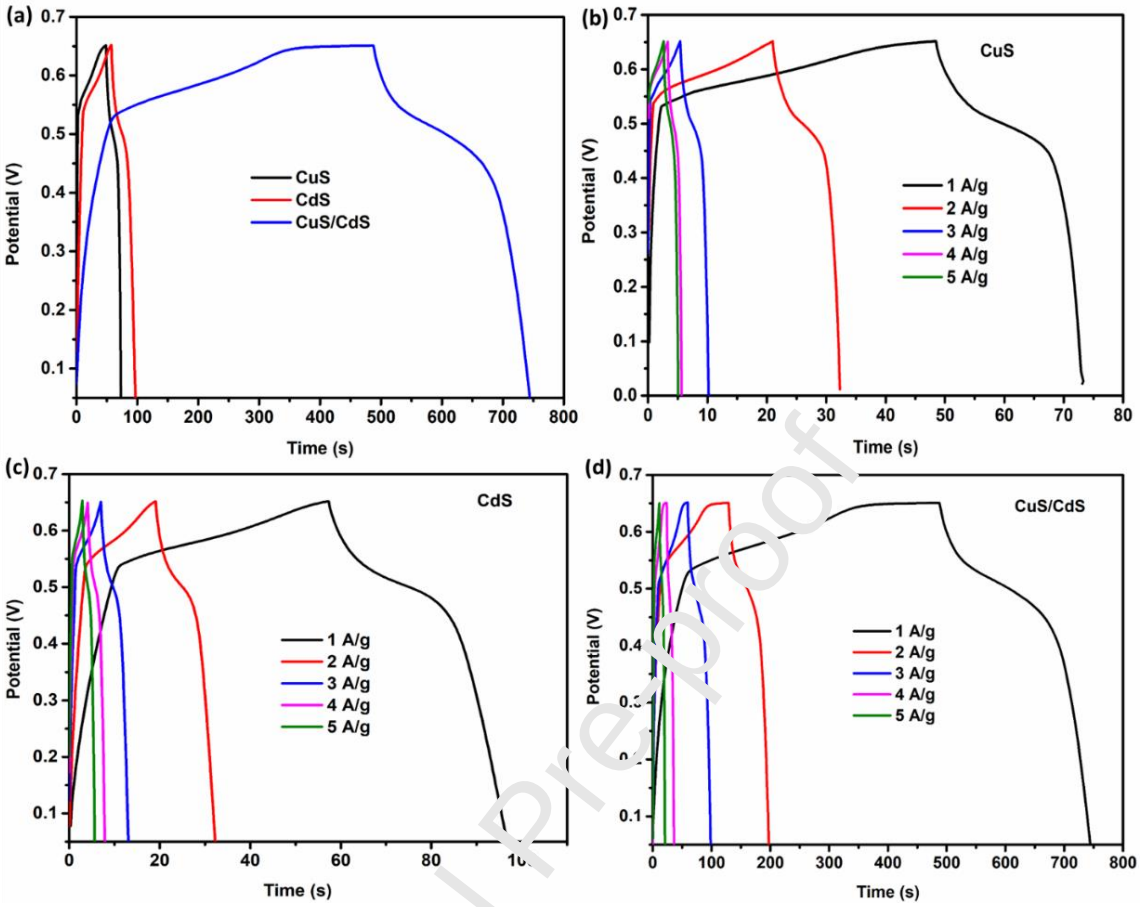

Fig. 9. (a) A comparison of the GCD curves of the CuS, CdS, and CuS@CdS nanocomposite at a current density of 1 Ag^{-1}. Galvanostatic charge/discharge behavior of (b) CuS, (c) CdS (d) and CuS@CdS nanocomposite at various current densities (1-5 Ag^{-1}).

Electrochemical impedance spectroscopy (EIS) is elucidated to comprehend the electrical conductivity and reaction kinetics at electrode/electrolyte interfaces of electrode materials. Fig. 10 (b) illustrates the Nyquist plot of the CuS, CdS, and CuS@CdS nanocomposite, which was obtained in the frequency range of 100 kHz to 0.01 Hz. Generally, the Nyquist plot shows three significant areas, the high, middle, and low frequency regions. The Nyquist plot is used for analyzing four different resistive parameters, including the solution resistance (Rs), the charge-transfer resistance (Rct), the equivalent series resistance (ESR) and Warburg resistance (W), which are the key factors in the analytical process. In terms of defining the semicircle, the starting point is indicated Rs, the closing point denoted as Rct, and the slope of the inclined line at 45° is indicated W. The calculated Rs value of CuS@CdS nanocomposite is (1.068 Ω) which

is lower than that of CuS (1.469 Ω) and CdS (1.373 Ω), its confirming that the lower resistance of the composite materials. An ESR is defined as the difference between the charge transfer resistance and the solution resistance. It can be calculated as follows: (ESR = Rct-Rs). It has been observed that the resistance values of CuS/CdS composites are much lower in comparison to CuS and CdS nanoparticles. In addition, this study confirmed that the synergistic effect of CuS and CdS nanoparticles increases the electrical conductivity. The enhanced electronic conductivity of CuS@CdS nanocomposite favorable charge transfer kinetics and the capacitance of the electrode materials during the faradic process [39].

The cyclic stability of the electrode materials is one of the prominent characteristics of commercial supercapacitor applications. The prolonged cyclic stabilities of the materials were obtained from charging and discharging tests for over 10000 cycles at a current density of 5 Ag^{-1}, which is depicted in Fig.10 (c). After this duration, the specific capacitance retention value of CuS@CdS nanocomposite was found to be 89.06% of its initial capacitance value, while the CuS and CdS electrodes can remain only (81.64%) and (80.76%) respectively. The high rate of capacity retention of CuS@CdS nanocomposite due to the internal architecture of the materials and the presence of the CdS nanoparticles enhances the mechanical stability as well as prolonged cyclic stability. Fig.10 (d) depicts the coulombic efficiency of the above-mentioned materials analyzed, and CuS@CdS nanocomposite demonstrates outstanding efficiency [40].

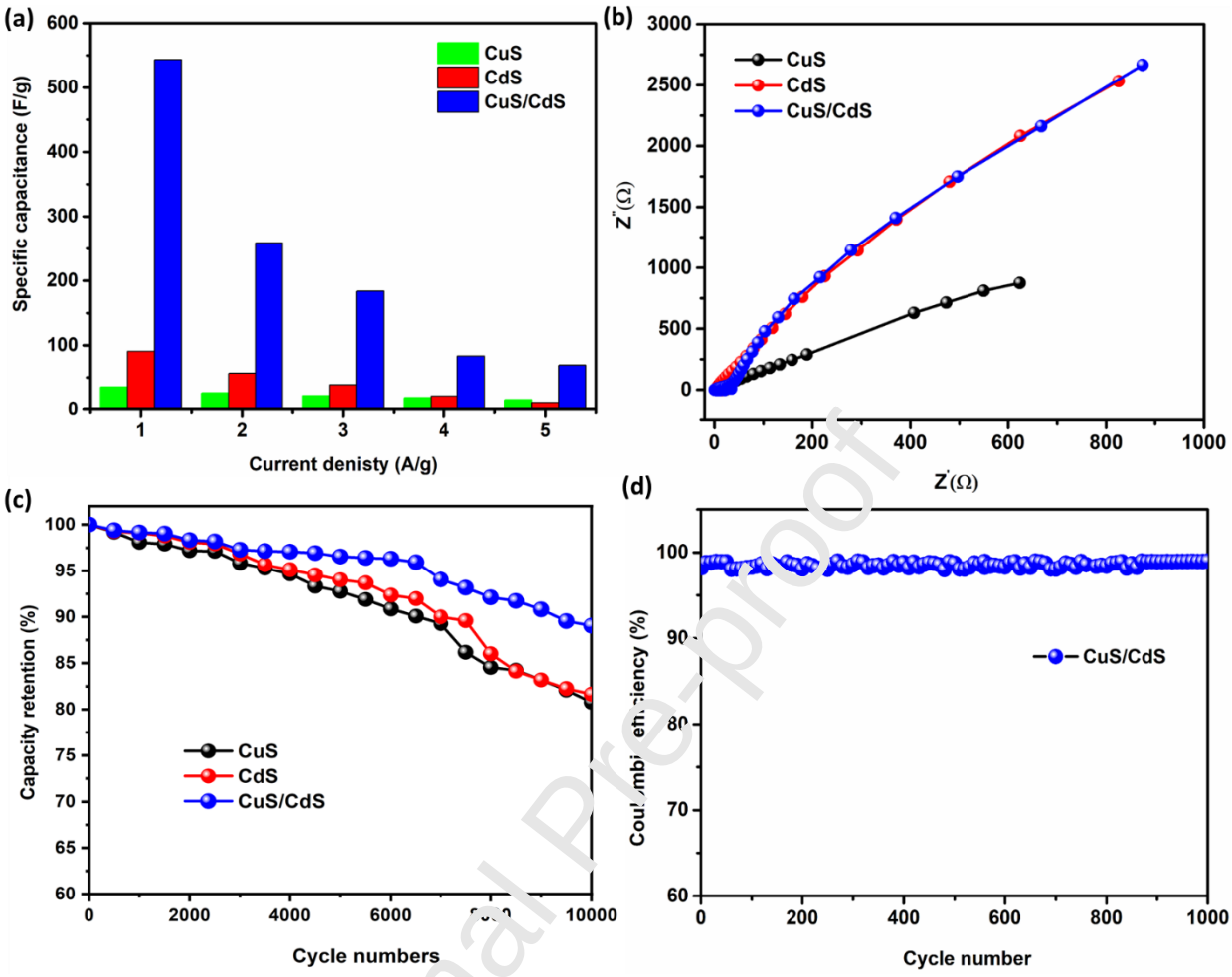

Fig.10. (a) Specific capacitance of all three materials over various current density, (b) EIS profile of CuS, CdS and CuS/CdS nanocomposite, (c) Cyclic stability of CuS, CdS and CuS/CdS nanocomposite, and (d) Columbic efficiency of CuS/CdS nanocomposite.

3.4. Electrochemical performance of all-solid-state asymmetric supercapacitor

An all-solid-state asymmetric supercapacitor device has been designed for the commercial application of CuS@CdS nanocomposite electrode. Asymmetric supercapacitors were constructed employing two different types of materials, such as activated carbon and metal sulphide nanocomposite, to enhance the electrochemical characteristics of the device. The electrochemical properties of activated carbon were investigated, and the associated results are shown in Fig. S1. As shown in Fig. S1 a, the CV curves of activated carbon were evaluated using a potential window of (-1-0 V) at different scan rates. This result suggests that activated carbon

exhibits electric double-layer capacitive behaviour, and slight humps were seen as a result of oxygen functional groups being present on the surface of the carbon. The same potential window is used to examine the galvanostatic charge/discharge properties of AC at various current densities. The GCD analysis was used to determine the specific capacitance of the AC, with the highest capacitance being 151.3 Fg^{-1} for 1 A/g. EIS was used to assess the materials' conductivity and reaction kinetics, which is shown in Fig.S1(d).

The construction of an all-solid-state asymmetric supercapacitor device would be AC/NF||PVA-KOH||CuS@CdS/NF, in which the activated carbon AC/NF as an anode material, CuS@CdS/NF cathode materials and PVA-KOH gel electrolyte act as a separator. According to charge balance theory, the mass ratio of the materials was calculated and kept to 1:3. The CV curves of the anode (-1-0 V) and cathode (0.0-.65 V) materials in the half-cell method were used to establish the device's potential window. Fig. 11 (a) reveals the comparison CV curves of AC and CuS@CdS nanocomposites, from this result AC demonstrates the electric double-layer capacitive behaviour and CuS@CdS nanocomposites show pseudocapacitive behaviour. It's interesting to note that the capacitive behaviours of the anode and cathode materials expand the operating potential window range for the device to up to 1.6 V. The potential window of the device was optimized at 1.6 V which is well-matched with a theoretically expected value. The CV test of the device was performed at different scan rates from 5-100 mVs^{-1} in the potential range of 0.0-1.6 V. Fig 11 (b) shows the obtained CV curves indicating the combination of both capacitive behaviours and also the same shape from low to high scan rates, this demonstrates the excellent reversibility of the electrode materials. In addition, the charge-discharge behaviours of the device were measured at various current densities, which are shown in Fig.11(c). The obtained curve shows an asymmetrical shape which is the influence of Faradaic charge transfer reactions. The specific capacitances of the ASC device were calculated from the CGD curve using eq (3), the obtained specific capacitance is given in Table.S2, and the corresponding figure shows in Fig.11(d). Furthermore, the power and energy densities were calculated at different current densities according to equations (4) and (5), the obtained results are given in Table.S2. The obtained results demonstrate high energy and power densities compared with previously reported asymmetric supercapacitor devices, which are given in the Ragone plot and summarized in Fig. 11 (e) and Table. 2. The Nyquist plot was performed to analyze the charge transfer kinetics between electrode and electrolyte, and the obtained values and the corresponding

equivalent circuit are depicted in Fig. 11 (f). The obtained values are indicating the lower resistance, high electronic conductivity and fast transfer kinetics between electrode and electrolyte due to the synergetic effect and morphology of the CuS/CdS nanocomposite. Furthermore, prolonged cyclic stability is a critical requirement for asymmetric supercapacitor devices. Fig. 11 (f) demonstrates the cyclic performance of the device at a current density of 5 A g^{-1}. The obtained result reveals outstanding cycling stability up to 95.5% after 3000 cycles, which is higher than compared to the reported materials.

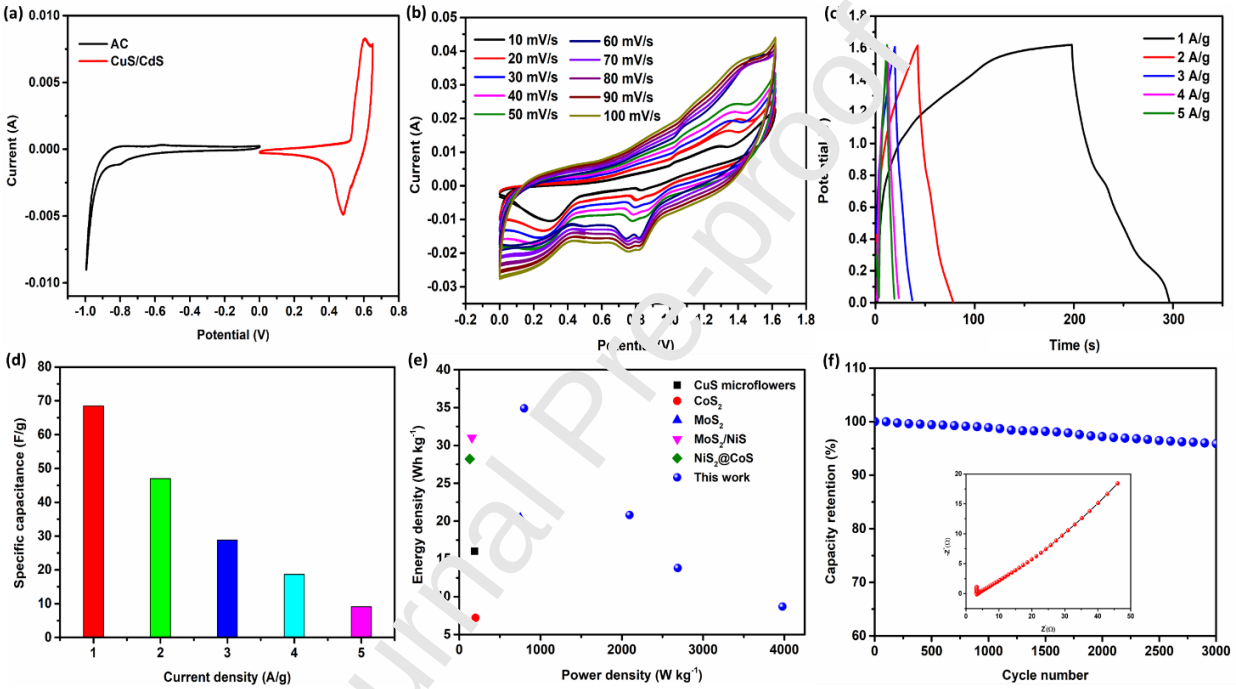

Fig.11. (a) CV curves of the CuS/CdS and AC electrodes at 10 mVs^{-1}, (b) CV curves of the ASC device (c) GCD profiles of the ASC device, (d) Specific capacities of ASC device, (e) Ragone plots of assembled ASC and reported literature, and (f) Cycling stability of the ASC device at 10 Ag^{-1} (inset shows the Nyquist plots of ASC).

Table. 2. The comparison of asymmetric CuS@CdS//AC device with reported literature results.

S.No.	Material	Energy density ($A\ g^{-1}$)	Power density ($A\ g^{-1}$)	Ref
1.	CuS hollow micro flowers	16	190	[41]
2.	CoS_2	7.2	200	[42]
3.	MoS_2//AC	20.42	750.31	[43]
4.	MoS_2/NiS//AC	31	155.7	[44]
5.	Ni_3S_2@CoS	28.2	130	[45]
6.	**CuS/CdS**	**34.9**	**698.1**	**This work**

4. CONCLUSIONS

In conclusion, we have successfully synthesized CuS@CdS heterostructure nanocomposite by a facile hydrothermal method for commercial supercapacitor devices. The XRD result of the nanocomposite demonstrated that the two types of metal sulfides CuS and CdS were observed. As an electrode material, CuS@CdS nanocomposite exhibited excellent electrochemical performance such as high specific capacitance and prolonged cyclic stability due to the various oxidation states, unique morphology and higher surface area. In addition, the all-solid-state asymmetric supercapacitor device delivered a high-power density of 798.1 ($W\ kg^{-1}$) and energy density of 34.9 ($Wh\ kg^{-1}$), along with outstanding cyclic stability of 94.07 % retention after 5000 cycles. These results suggest that CuS@CdS nanocomposite can hold great promise for commercialization in the supercapacitor device.

CRediT authorship contribution statement

Ranjith Balu: Validation, Investigation, Writing-original draft, Methodology, Writing-review & editing, Visualization. Anthoniammal Panneerselvam: Writing-review & editing. R. Jothi Ramalingam: Resources, Writing-original draft, Writing-review & editing, Visualization. Gautham Devendrapandi: Writing-original draft, Writing-review & editing. Surender Subburaj: Formal analysis. S. Anand: Formal analysis. Uma shankar Veerasamy: Writing - review & editing**.** Suganya Palani: Writing - review & editing**.**

Acknowledgement

The authors acknowledge the financial support through Researchers Supporting Project number (RSP2023R 354), King Saud university, Riyadh 11451, Saudi Arabia

Corresponding Author

Ranjith Balu- Department of Physics, Saveetha School of Engineering, Saveetha Institute of Medical and Technical Sciences (SIMATS), Thandalam, Chennai, Tamil Nadu, India,

Email: rbalubio@gmail.com

REFERENCES:

[1] Antonio Sánchez, Qi Zhang, Mariano Martín, Pastora Vega, Towards a new renewable power system using energy storage: An economic and social analysis, Energy Conversion and Management, Vol. 252, (2022), pp. 115056. https://doi.org/10.1016/j.enconman.2021.115056.

[2] Pawan Saini, Lata Gidwani, 'An investigation for battery energy storage system installation with renewable energy resources in distribution system by considering residential, commercial and industrial load models', Journal of Energy Storage, Vol (45), 2022, pp.103493. https://doi.org/10.1016/j.est.2021.103493.

[3] Lu Feng, Xinjing Zhang, Xiaoyu Li, Bin Li, Yang Li, Yujie Xu, Huan Guo, Xuezhi Zhou, Haisheng Chen, Performance analysis of hybrid energy storage integrated with

distributed renewable energy, Energy Reports, Vol 8, 2022, pp. 829-1838. https://doi.org/10.1016/j.egyr.2021.12.078.

[4] S. Ould Amrouche, D. Rekioua, T. Rekioua, S. Bacha, Overview of energy storage in renewable energy systems, International Journal of Hydrogen Energy, Vol. 41, (45), 2016, pp. 20914-20927.https://doi.org/10.1016/j.ijhydene.2016.06.243.

[5] A.G. Olabi, Renewable energy and energy storage systems, Energy, Vol.136, 2017, pp. 1-6. https://doi.org/10.1016/j.energy.2017.07.054.

[6] Qiao, L.; Zhang, X.; Sun, X.; Zhang, X.; Ma, Y. Advances in Battery-Supercapacitor Hybrid Energy Storage System. Energy Stor. Sci. Technol. 2022, 11, pp. 98–106. https://doi.org/10.1016/j.energy.2017.07.054.

[7] Guang Cong Zhang, Man Feng, Qing Li, Zhuang Wang, Zixun Fang, Zhimin Niu, Nianrui Qu, Xiaoyong Fan, Siheng Li, Jianmin Gu, Jidong Wang, and Desong Wang, High Energy Density in Combination with High Cycling Stability in Hybrid Supercapacitors, ACS Appl. Mater. Interfaces 2022, 14, 2, 2674–2682. https://doi.org/10.1021/acsami.1c17285.

[8] Ramkrishna Sahoo, Tae Hoon Lee, Duy Tho Pham, Thi Hoai Thuong Luu, and Young Hee Lee, Fast-Charging High-Energy Battery–Supercapacitor Hybrid: Anodic Reduced Graphene Oxide–Vanadium(IV) Oxide Sheet-on-Sheet Heterostructure, ACS Nano 2019, 13, 9, 10776–10786. https://doi.org/10.1021/acsnano.9b05605.

[9] Katayoon Gholami laelabadi, Rostam Moradian, Iraj Manouchehri. Facile Method of Fabricating Interdigitated and Sandwich Electrodes for High-Performance and Flexible Reduced Graphene Oxide@Polyaniline Nanocomposite Supercapacitors. ACS Applied Energy Materials 2021, 4 (7), 6697-6710. https://doi.org/10.1021/acsaem.1c00754.

[10] Zi-Hang Huang, Si-Jia Du, Yue Zhang, Tianyi Ma, Hui Li. A high-performance vanadium oxide@molybdenophosphate composite for 2.2 V aqueous symmetric supercapacitors. Chemical Engineering Journal 2022, 449, 137750. https://doi.org/10.1016/j.cej.2022.137750.

[11] Syed Shaheen Shah, Md. Abdul Aziz, Zain H. Yamani. Recent Progress in Carbonaceous and Redox-Active Nanoarchitectures for Hybrid Supercapacitors: Performance Evaluation, Challenges, and Future Prospects. The Chemical Record 2022, 22 (7) https://doi.org/10.1002/tcr.202200018.

[12] Rika Taslim, Apriwandi Apriwandi, Erman Taer, Novel Moringa oleifera Leaves 3D Porous Carbon-Based Electrode Material as a High-Performance EDLC Supercapacitor, ACS Omega. 2022 Oct 9;7(41):36489-36502. doi: 10.1021/acsomega.2c04301.

[13] Mohd Asyadi Azam, Nik Suhaini Nik Ramli, Nurul Aini Nadirah Mohd Nor, Tuan Idzuddin Tuan Nawi, Recent advances in biomass-derived carbon, mesoporous materials, and transition metal nitrides as new electrode materials for supercapacitor: A short review, Int. J. Energy Res, Vol. 45, (6) Special Issue: Progress in Alternative Fuels and Energies, 2021. Pp. 8335-8346. https://doi.org/10.1002/er.6377.

[14] D. Qu, H. Shi, Studies of activated carbons used in double-layer capacitors, J. Power Sources, 74 (1) (1998), pp. 99-107. https://doi.org/10.1016/S0378-7753(98)00038-X.

[15] Long Liu, Huaping Zhao, Yong Lei, Review on Nanoarchitecture Current Collectors for Pseudocapacitors, Small, Vol. 3, 8, 2019, https://doi.org/10.1002/smtd.201800341.

[16] Z. Shi, S. Wei, H. Zuo, M. Huang, J. Shi, H. Wang, Boosting capacitance and energy density by construction $NiCoO_2/CoS_2$ nanocomposites arrays as pseudocapacitor, J. Alloys Compd., 881 (2021), 160627-1800341. https://doi.org/10.1016/j.jallcom.2021.160627.

[17] M. Cui, X. Meng, Overview of transition metal-based composite materials for supercapacitor electrodes, Nanoscale Adv., 2 (2020), pp. 5516-5528.

[18] Yanqun Tang, Wenhan Guo, Ruqiang Zou, Nickel-based bimetallic battery-type materials for asymmetric supercapacitors, Coordination Chemistry Reviews, Vol.451, (15), 2022, pp. 214242.

[19] Xin-Yao Yu, Le Yu, Xiong Wen (David) Lou, Metal Sulfide Hollow Nanostructures for Electrochemical Energy Storage, Vol. 6, (3), 2016,1501333. https://doi.org/10.1002/aenm.201501333.

[20] R. Balu, S. Sagedevan, A. Dakshanamoorthy, A Cost Effective, Facile Hydrothermal Approach of Zinc Sulfide Decorated on Graphene Nanocomposite for Supercapacitor Applications, Volume 19, 11, (2019), pp. 6987-6994(8). https://doi.org/10.1166/jnn.2019.16670.

[21] R. Balu, A. Dakshanamoorthy A Simple Hydrothermal Synthesis of Cadmium Sulfide Wrapped on Graphene Nanocomposite for Supercapacitor Applications. J Nanosci Nanotechnol. 21(12) (2021) 5835-5845. doi: 10.1166/jnn.2021.19503.

[22] R. Balu, A. Dakshanamoorthy, A facile one-pot hydrothermal synthesis of cobalt sulfide nanospheres integrated with graphene nanocomposite as electrode material for high-performance supercapacitors, J. Mater. Sci. Mater. Electron. 33 (13) (2022) 10057–1007,

[23] R. Balu, A. Dakshanamoorthy, Synthesis of wool ball-like copper sulfide nanospheres embedded graphene nanocomposite as electrode for high performance symmetric supercapacitor device. Int. J. Energy Res. 24, 1–15 (2021).

[24] Kummara Venkata Guru Raghavendra, Kummara Madhusudana Rao, N.T. Uday Kumar, Hydrothermal synthesis of CuS/CoS nano composite as an efficient electrode for the supercapattery applications, Journal of Energy Storage, Vol. 40, 2021, pp.102749. https://doi.org/10.1016/j.est.2021.102749.

[25] Huiyin Liu, Zuoxing Guo, Xiaobing Wang, Jin Hao, Jianshe Lian, CuS/MnS composite hexagonal nanosheet clusters: Synthesis and enhanced pseudocapacitive properties, Electrochimica Acta, Vol. 271, 1 (2018), pp. 425-432. https://doi.org/10.1016/j.electacta.2018.03.048.

[26] Ming-Hui Sun, Ming-Yu Qi, Zi-Rong Tang, Yi-Jun Xu Dual cocatalysts decorated CdS nanoparticles for efficient dehydrocoupling of thiols into disulfides, Applied Catalysis B: Environmental, Vol.321, 2023, pp.122019. https://doi.org/10.1016/j.apcatb.2022.122019.

[27] Pan He, Ling Zhang, Linzhen Wu, Xin Yang, Tao Chen, Yi Li, Xiaoyong Yang, Lin Zhu, Qi Meng, Tao Duan. Synergistic Effect of the Sulfur Vacancy and Schottky Heterojunction on Photocatalytic Uranium Immobilization: The Thermodynamics and Kinetics. Inorganic Chemistry 2022, 61 (4), 2242-2250. https://doi.org/10.1021/acs.inorgchem.1c03552.

[28] Enhanced photocatalytic degradation of methylene blue dye using CuS-CdS nanocomposite under visible light irradiation Appl. Surf. Scien., 475 (2019), pp. 828-838, 10.1016/j.apsusc.2018.12.178.

[29] Alexander G. Milekhin, Nikolay A. Yeryukov, Larisa L. Sveshnikova, Tatyana A. Duda, Ekaterina E. Rodyakina, Victor A. Gridchin, Evgeniya S. Sheremet and Dietrich R. T. Zahn, Combination of surface- and interference-enhanced Raman scattering by CuS nanocrystals on nanopatterned Au structures, Beilstein J. Nanotechnol. 6 (2015), pp. 749–754. https://doi.org/10.3762/bjnano.6.77.

[30] N. Tschirner, H. Lange, A. Schliwa, A. Biermann, C. Thomsen, K. Lambert, R. Gomes, Z. Hens, Interfacial alloying in CdSe/CdS heteronanocrystals: a Raman spectroscopy analysis, Chem. Mater. 24 (2012) 311–318.

[31] Yuehu Wana, Shiwen Dub, Congrong Lua, Kuankuan Rena, Biyun Shia, Shiyan Liua, Chunhe Lia, Weidong Dona, Ping Fanga, Na Ye, Metallic CuS decorated CdS nanowires for efficient photocatalytic H_2 evolution under visible-light irradiation, Journal of Alloys and Compounds 871 (2021), pp. 159461.

[32] J.R. Jayaramaiah, V. Jayanth, Shamanth Ramaswamy, Structural Elucidation and Optical Analysis on Europium Doped Cadmium Sulphide Nano Thin Films, Optik - International Journal for Light and Electron Optics 208(1019), pp.164079. 10.1016/j.ijleo.2019.164079.

[33] Chandrasekaran Nithya and Gowtham Thiyagaraj, Morphology oriented CuS nanostructures: superior K-ion storage using surface enhanced pseudocapacitive effects, Sustainable Energy Fuels, 2020,4, 3574-3587.

[34] An-Qi Zhang, Qing-Zhe Tan, Hui-Jun Li, Li Sui, Dong-Jin Qian & Meng Chen, pH-Dependent shape changes of water-soluble CdS nanoparticles, Journal of Nanoparticle Research volume 16, Article number: 2197 (2014).

[35] M. Ahmad Pandit, S. Billakanti, K. Muralidharan, A simplistic approach for the synthesis of CuS-CdS heterostructure: A novel photo catalyst for oxidative dye degradation, J. Environ. Chem. Eng. 8 (2) (2020) 103542.

[36] L. Ge, F. Zuo, J. Liu, Q. Ma, C. Wang, D. Sun, L. Bartels, P. Feng, Synthesis and efficient visible light photocatalytic hydrogen evolution of polymeric g-C_3N_4 coupled with CdS quantum dots, J. Phys. Chem. C 116 (2012) 13708–13714, https://doi.org/10.1021/jp3041692.

[37] M. Mahanthappa, N. Kottam, S. Yellappa, Enhanced photocatalytic degradation of methylene blue dye using CuS-CdS nanocomposite under visible light irradiation, Appl. Surf. Scien. 475 (2019) 828–838, https://doi.org/10.1016/j.apsusc.2018.12.178.

[38] Ranjith Balu, Arivuoli Dakshanamoorthy, One pot preparation of tin sulfide decorated graphene nanocomposite for high performance supercapacitor applications, Inorganic Chemistry Communications, Vol.136, (2022), 109148. https://doi.org/10.1016/j.inoche.2021.109148.

[39] Tingkai Zhao, Xiarong Peng, Xin Zhao, Jingtian Hu, Wenbo Yang, Tiehu Li, Ishaq Ahmad Facile preparation and high capacitance performance of copper sulfide microspheres as supercapacitor electrode material, Composites Part B: Engineering, Vol.163, 15, (2019), pp.26-35. https://doi.org/10.1016/j.compositesb.2018.11.023.

[40] Ranjith Balu, Saravanan Krishna Sundaram, Sundaramurthy Rameshkumar, Karuppannan Aravinth, Perumalsamy Ramasamy, Controlled growth of 2D structured Cu2WS4 nanoflakes for high-performance all-solid-state supercapacitors, Journal of Electroanalytical Chemistry, Vol. 922, 1, (2022), 116718. https://doi.org/10.1016/j.jelechem.2022.116718.

[41] Liu Y, Zhou Z, Zhang S, Luo W, Zhang G. Controllable synthesis of CuS hollow microflowers hierarchical structures for asymmetric supercapacitors. Appl Surf Sci 2018; 422:711–9.

[42] Ren R, Faber MS, Dziedzic R, et al. Metallic CoS_2 nanowire electrodes for high cycling performance supercapacitors. Nanotechnology 2015;26(49). 494001.

[43] Tsung-Wu Lin, Min-Chien Hsiao, Ai-Yin Wang, Jeng-Yu Lin Hollow Hierarchical Carbon Spheres Decorated with Ultrathin Molybdenum Disulfide Nanosheets as High-Capacity Electrode Materials for Asymmetric Supercapacitors, Chemelectrochem, Vol. 4, (2017), Pp.620-627.

[44] Q. Qin, L. Chen, T. Wei, X. Liu, MoS_2/NiS yolk–shell microsphere-based electrodes for overall water splitting and asymmetric supercapacitor, Small 15 (2019) 803639.

[45] Li R, Wang S, Wang J, Huang Z. Ni_3S_2@CoS core-shell nano-triangular pyramid arrays on Ni foam for high-performance supercapacitors. Phys Chem Chem Phys, 2015;17(25):16434–42.

CRediT authorship contribution statement

Ranjith Balu: Validation, Investigation, Writing-original draft, Methodology, Writing-review & editing, Visualization. **Anthoniammal Panneerselvam**: Writing-review & editing. **R. Jothi Ramalingam**: Resources, Writing-original draft, Writing-review & editing, Visualization. **Gautham Devendrapandi**: Writing-original draft, Writing-review & editing. **Surender Subburaj**: Formal analysis. **S. Anand**: Formal analysis. **Uma shankar Veerasamy**: Writing - review & editing**. Suganya Palani**: Writing - review & editing**.**

Declaration of Competing Interest

The authors declare that they have no known competing financial interests or personal relationships that could have appeared to influence the work reported in this paper.

Graphical Abstract

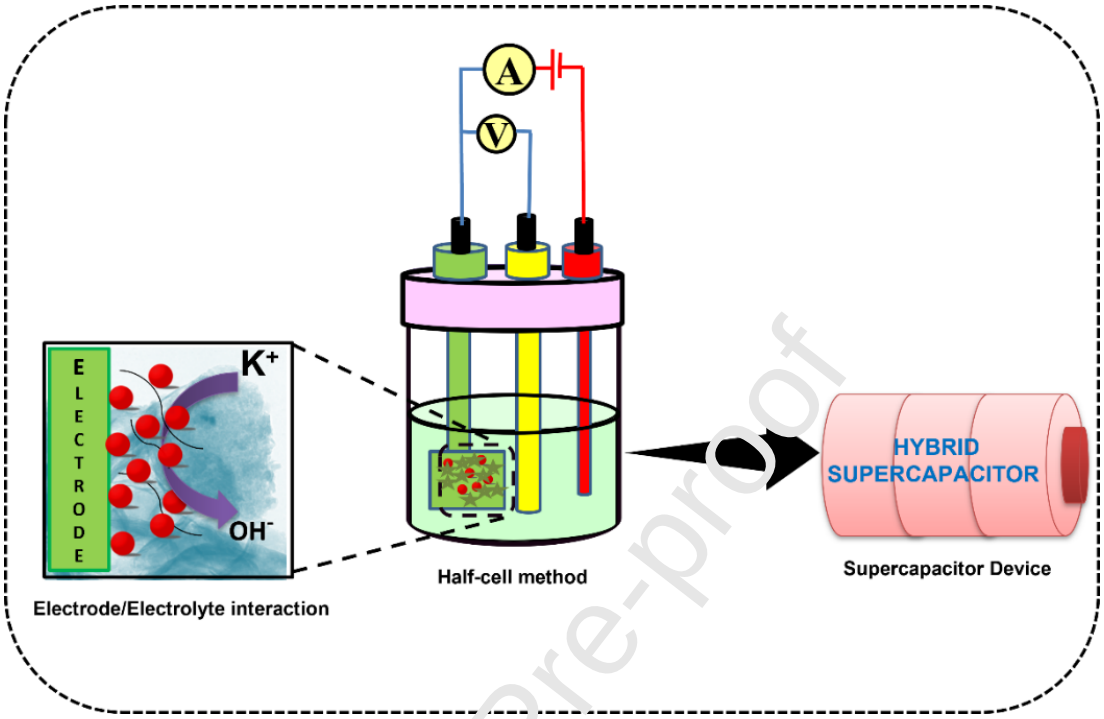

Highlights

- Heterostructure CuS/CdS nanocomposite was prepared by simple hydrothermal method
- Heterostructure CuS/CdS nanocomposite reveals unique Echinops flower-like morphology
- The CuS/CdS nanocomposite demonstrates excellent specific capacitance of 543.6 F g^{-1} as well as outstanding cycling stability compare than CuS and CdS nanoparticles.